Bound states in the continuum via singular transfer matrices

Ovidiu-Zeno Lipan [*]

Department of Physics, Gottwald Center for the Sciences 138 UR Drive, University of Richmond, Richmond, Virginia 23173, USA

Aldo De Sabata

Department of Measurements and Optical Electronics,
Politehnica University of Timisoara, Bd. V. Pârvan, No. 2, 300006 Timisoara, Romania

Bound states in the continuum (BICs) in photonic crystal slabs are Bloch eigenstates with zero linewidth and infinite lifetimes, though practical devices exhibit quasi-BICs due to geometric imperfections and material losses. Despite these limitations, quasi-BICs still maintain high Q factors, enabling applications in lasing, high harmonic generation, and biosensing. The selection of specific geometrical or material parameters is essential to achieve devices that sustain BICs. Our work presents a framework for generating BICs by driving the transfer matrix of a device to a singular point, where it becomes noninvertible, thus defining the BIC states. This method applies to nonhomogeneous, tessellated structures and is supported by closed-form analytical expressions, facilitating efficient parametric exploration. The proposed framework aligns with the conjecture that the most robust BICs are associated with topological defects in specific parameter spaces. We identify regions in parameter space supporting BICs and validate our theoretical predictions through full-wave numerical simulations. The framework extends to a wide range of photonic structures, enabling robust design and optimization of devices for diverse applications.

I. INTRODUCTION

Bound states in the continuum (BICs) in photonic crystal slabs are Bloch eigenstates extended in the slab's plane but spatially evanescent in the direction orthogonal to the slab. These states are Fano resonances with zero linewidth and infinitely extended lifetimes [1–3]. The Q factor becomes finite in fabricated devices due to the finite size of the crystal, losses in the dielectric material, or geometric imperfections. Nevertheless, it remains sufficiently high, resulting in the formation of a quasi-BIC.

Applications include lasing from a BIC cavity [4], a significant enhancement in high harmonic generation driven by resonant modes associated with quasi-BIC states [5], and high-Q resonant dielectric BIC metasurfaces for biosensing platforms [6], among many others [7].

BICs are usually classified as symmetry protected [8–10] or accidental [11,12].

Symmetry-protected BICs are governed by a robust structural constraint–symmetry–that prevents radiation leakage. In contrast, accidental BICs depend on a fine balance of parameters, which can be easily disturbed. However, in both cases, certain geometrical or material parameters must be selected to either achieve intrinsic symmetry or fine-tuning [13]. This intricate relationship between BICs and structural parameters is part of a broader exploration [14,15], where the dependence on such parameters in photonic systems mirrors the general concept of physical states forming families in parameter space. Just as understanding the surfaces that

separate different phases or states in other areas of physics is key to control and prediction, the emergence of BICs under specific parameter conditions in photonic systems similarly demonstrates the need for accurate parameter selection.

Our work is driven by the goal of distinguishing families of surfaces in parameter space that describe devices capable of generating BICs. The criteria for selecting these special surfaces focus on identifying where the device's transfer matrix becomes singular. We position our approach in the same realm as the conjecture in Refs. [1,16], where it was proposed that the most robust BICs correspond to topological defects in specific parameter spaces.

The singularity of the transfer matrix is nontrivial, as we move beyond the use of homogeneous layers with constant permittivity, where the transfer matrix is typically applied to photonic crystal slabs, and instead focus on devices employing nonhomogeneous, polygonally tessellated patterned laminae [17], making our approach applicable to a wide range of photonic structures.

Moreover, the elements of the transfer matrix are derived as closed-form analytical expressions [18] allowing the singularity surfaces to also be realized in closed form. Closed-form surfaces are advantageous in practical applications due to their computational efficiency and design versatility, particularly in avoiding large-scale simulations or iterative optimization processes. Closed-form solutions also facilitate parametric analysis, enabling efficient exploration of system behavior under varying conditions. This simplicity enhances the ability to identify optimal configurations in both design and experimental implementation.

We begin in Sec. II by selecting a device to realize the transfer matrix, which is then driven to a singular point in

---

[*]Contact author: olipan@richmond.edu

Sec. III, as demonstrated in Eq. (11), Eq. (12), Figs. 2, and 3.

At this singular point, the transfer matrix is not invertible, and thus the scattering matrix lacks clear definition. This singularity is linked to BIC states, which correspond to the null space of the transfer matrix at the singular point, as emphasized in the discussions of Eqs. (19) and (20) from Sec. IV. We identified two frequency regions: one that hosts a pair of BICs, Sec. V, and another where a resonance and a BIC coexist, Sec. VII. In the vicinity of such a singular point, the scattering matrix is well defined in Eqs. (24)–(26), giving rise to quasi-BIC states in Eq. (33), Sec. VI.

The behavior of BICs is closely tied to the structure of the scattering matrix elements, with the positions of poles and zeros in the complex plane playing a fundamental role. As parameters vary, the movement of these poles and zeros, as shown in Figs. 7 and 9, directly influences the properties of BICs and the transmission of the incoming mode.

The theoretically predicted properties of the BICs, some of which were computed using [19], are validated through full-wave numerical simulations [20], as shown in Figs. 8 and 12. We study the robustness of the findings as the dimension of the linear space of modes, and consequently the dimension of the transfer matrix, increases, Fig. 11.

The robustness to potential variations in the device's fabrication geometry is demonstrated in Fig. 13, indicating that the properties are preserved in the vicinity of the point representing the selected device on the theoretical surface shown in Fig. 2.

The framework presented in this manuscript, which utilizes a singular transfer matrix to create BICs, can be extended to a broader class of devices with geometries and material properties significantly different from those selected in this work.

II. DEVICE

To materialize the transfer matrix and to illustrate the point above, we had the option to utilize various polygonal shapes to construct a device for study, such as the one depicted in Fig. 1 of Ref. [17]. Nevertheless, we opted for the device shown in Fig. 1, given its frequent utilization [21–23]. The device is finite along the z axis, having a thickness denoted by l_z, but periodically infinite in the x and y directions.

The transfer matrix maps the electromagnetic field from position z min to z max. We set $z_{\min}$ at $l_z/4$, in vacuum, on one side of the device, and transferred the field to $z_{\max}$, also at $l_z/4$ in vacuum, but on the other side of the device, from the negative to the positive z directions, respectively, as shown in Fig. 1. The specific positions of z min and z max are connected to the space discretization proposed in Ref. [24], set here to half the device thickness, $l_z/2$. This discretization is appropriate, as it aligns with the thin-lamina structure of the devices under consideration.

The labeling structure of the transfer matrix is hierarchically nested, with each level contained within the one above [18]. The first level reveals a 4×4 grid where each block exhibits the matrix elements that couple between the (−) and
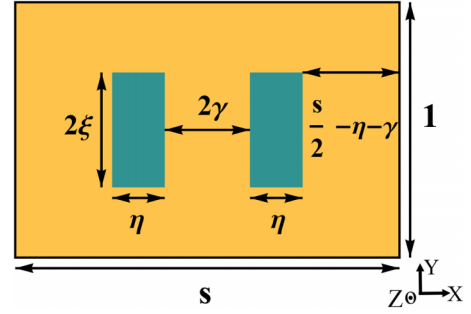

FIG. 1. To illustrate the core concepts, we have chosen this type of geometry, although any bilaminar tessellated polygonal shape could be used. All the geometrical data are unitless, scaled by l_y, the unit cell's vertical edge. To obtain the geometry in the chosen units, multiply all geometrical parameters by l_y. The two holes, symmetrically placed with respect to the center of the unit cell, have relative permittivity $\epsilon = 1$, whereas the surrounding is silicon of $\epsilon_B = 11.9$. The unit cell is not necessarily a square, which is evident when $s \neq 1$. In this study, we opt to work with $s = 1$. We will then explore the case $s \neq 1$ and investigate an accidental BIC in a separate publication.

(+) propagation directions along the z axis:

$$T = \begin{bmatrix} T^{+,+} & T^{+,-} \\ T^{-,+} & T^{-,-} \end{bmatrix}. \tag{1}$$

The remaining labels associated with each element of the $T^{\pm,\pm}$ matrix specify the polarization and the Bloch-Floquet mode (BF) defined as in Ref. [18]. Given the periodicity of the device in both the x and y directions, the transmitted and reflected fields can be expressed as a superposition of BF modes (M_x, M_y), where M_x and M_y can take any integer value. Throughout the paper, we will confine our discussion to TE polarization since the TM modes do not couple significantly into the TE. Consequently, the elements of each block matrix in Eq. (1) are identified by their respective BF indices.

The transmission scattering matrix, which takes input from location z-max and produces output at location z min, requires the inversion of the $T^{-,-}$ matrix

$$S^{\min,\max} = (T^{-,-})^{-1}. \tag{2}$$

Therefore, studying the singularities in transmission provides a natural starting point.

The computational process might appear deceptively simple at first glance. However, the ability of this approach to distill intricate analytical formulas into a concise form may be unexpected if not surprising.

III. GENERATING A SINGULAR TRANSFER MATRIX

The incident plane wave, characterized by the BF mode (0,0), travels from z max to z min. Its propagation direction is defined by the polar angle θ and the azimuthal angle φ, while the time dependence is $e^{-i\omega t}$.

In all the formulas that follow, the angular frequency is represented by a unitless parameter Ω defined as $\Omega = (l_z/2)(\omega/v_0)$, where v_0 is the speed of light in vacuum.

In the approach described below, we first ensure that the projection of the transfer matrix $T^{-,-}$ onto a lower-dimensional subspace spanned by a particular selection of

BF modes is singular. Subsequently, in Sec. VIII, we assess whether the BICs formed within a lower-dimensional subspace persist within a higher-dimensional one.

The lower-dimensional subspace employed is five-dimensional, with the BF modes ordered and numbered from 1 to 5 as follows: $(0, 0)$, $(-1, 0)$, $(1, 0)$, $(0, -1)$, and $(0,1)$. There is freedom in selecting the dimension of the lower-dimensional subspace, depending on the number of BICs we need to obtain. It turns out that we generate three BICs within this five-dimensional space.

There is a particular circumstance to consider when the angle θ approaches zero due to the specific structure of the BF basis we use. In particular, the vector (E_x, E_y, H_x, H_y), which represents the state of the electromagnetic field proposed in Ref. [24] and adopted in Ref. [18], has E_z and H_z left aside, as they are dependent on the other four components. As a consequence, the first vector of the BF basis, which is associated with the incoming mode $(0, 0)$, tends toward zero as θ diminishes. This happens because all of its components share a common factor of $\sin(\theta)$. To avoid working with a zero vector, we perform a change of basis by employing the subsequent diagonal matrix $U = \mathrm{diag}(\sin(\theta), 1, 1, 1, 1)$:

$$T^{-,-}|_{\text{new basis}} = U T^{-,-} U^{-1}. \tag{3}$$

In what follows we will not carry on the label "new basis" in the context of $\theta = 0$.

By employing the method presented in Ref. [18] to compute the analytical formulas for the transfer matrix we derive the following structure:

$$T^{-,-} = \begin{bmatrix} T_{11} & T_{12} & -T_{12} & 0 & 0 \\ T_{21} & T_{22} & T_{23} & 0 & 0 \\ -T_{21} & T_{23} & T_{22} & 0 & 0 \\ 0 & 0 & 0 & T_{22} & T_{45} \\ 0 & 0 & 0 & T_{45} & T_{22} \end{bmatrix}, \tag{4}$$

for the device from Fig. 1 at $\theta = 0$, $\varphi = 0$ and $s = 1$, making the unit cell of this thin device a square for the rest of this paper. The specific format outlined by Eq. (4) represents the manifestation of symmetry in the transfer matrix pertinent to the device class depicted in Fig. 1 with $s = 1$. Symmetries related to the Γ point are ubiquitous.

Driving the transfer matrix to a singular point necessitates additional constraints. Here, we propose to request that, at $\theta = 0$ and $\varphi = 0$, there exists a frequency Ω located on the real axis of the complex frequency plane such that

$$\det(T^{-,-}) = 0, \tag{5}$$

$$\mathrm{Cof}(T^{-,-})_{11} = 0, \tag{6}$$

where $\mathrm{Cof}(T^{-,-})_{11}$ is the cofactor of the element $T_{11}^{-,-}$ from the transfer matrix.

The reason behind this choice is that, for a well-defined scattering matrix, Eq. (2), the transmission of the incoming propagative mode $(0, 0)$ is

$$S_{11}^{\mathrm{min,max}} = \frac{\mathrm{Cof}(T^{-,-})_{11}}{\det(T^{-,-})}. \tag{7}$$

Through Eqs. (5) and (6), we establish the possibility for the transmission to have a finite, nonzero value in the limit

of $\theta \to 0$, akin to L'Hôpital's rule. Away from $\theta = 0$ where the cofactor and the determinant no longer share a common root, the transmission will be extinguished by the zero of the cofactor. The imposed conditions suggest the presence of a BIC where the transmission abruptly transitions from being zero at $\theta \neq 0$ to a nonzero value close to 1 at $\theta = 0$. This represents a key point in introducing a relevant singularity for generating BICs.

These two constraints typically necessitate their separation into real and imaginary parts, as our matrix elements are generally complex numbers. However, by exploiting the fact that transfer matrix elements are real numbers for the evanescent modes in lossless dielectric devices, we can reduce the number of equations needed to impose the singularity.

Out of several alternatives to satisfy Eqs. (5) and (6), we chose two relationships among the matrix elements,

$$T_{23} = T_{45}, \tag{8}$$

$$T_{23} = -T_{22}, \tag{9}$$

that not only ensure the validity of Eqs. (5) and (6) but also result in a shape for $T^{-,-}$,

$$T^{-,-} = \begin{bmatrix} T_{11} & T_{12} & -T_{12} & 0 & 0 \\ T_{21} & H & -H & 0 & 0 \\ -T_{21} & -H & H & 0 & 0 \\ 0 & 0 & 0 & H & -H \\ 0 & 0 & 0 & -H & H \end{bmatrix}, \tag{10}$$

that sustains a double real root in frequency for both the determinant and cofactor, which will produce two BICs. The constraint (9) extends the already existing relation $T_{13} = -T_{12}$, whereas (8) duplicates the 2×2 matrix of the BF modes 2 and 3 to the pair 4 and 5.

We have reached a decisive moment to leverage the analytic closed-form formulas for the transfer matrix elements [18], enabling us to simplify the first equation (8) to

$$\xi \sin(4\pi\gamma) - \xi \sin(4\pi(\gamma + \eta)) + \eta \sin(4\pi\xi) = 0, \tag{11}$$

whereas Eq. (9) gives

$$\eta\xi(1 - \mathrm{sinc}(4\pi\xi)) = \frac{1}{4} \frac{((\epsilon_B - 1)\Omega^2 \Phi_e - 1)^2 - (\Phi_e)^2}{((\epsilon_B - 1)\Omega^2 \Phi_e - 1)^2 - 1}, \tag{12}$$

with $\mathrm{sinc}(x) = x^{-1}\sin(x)$. Here Φ_e captures the propagation along the z axes of evanescent waves, as described in Ref. [18],

$$\Phi_e = \Phi_{Z,\text{evanescent}}\left(\tfrac{1}{2}(2 + w^2 - \Omega^2)\right), \tag{13}$$

with

$$\Phi_{Z,\text{evanescent}}(z) = z - \sqrt{z^2 - 1}, \tag{14}$$

$$w = l_z \pi. \tag{15}$$

Unless the dimensional units of l_z are specified, l_z will, from this point forward, be treated as a dimensionless quantity, defined, in accordance with the rule in Fig. 1, as the thickness along the z axis divided by the unit cell length along the y axis, l_y. In Eq. (15), which defines the width parameter w, l_z appears as a dimensionless quantity.
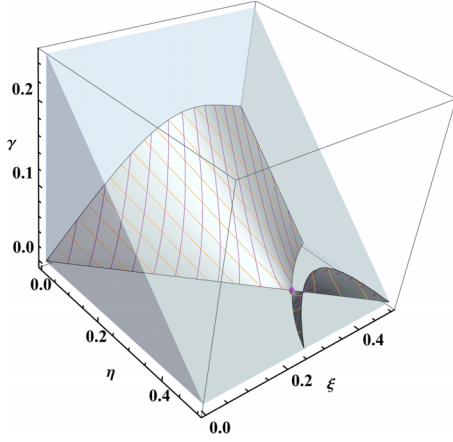
FIG. 2. The 3D surface for the BICs devices that fulfill the shape (10) and have a square unit cell, $s = 1$. Note that this surface does not depend on w from Eq. (15).

In this manuscript, when designing a specific device, we start by setting a value for w by choosing l_y and l_z, with $l_z \ll 1$ fulfilling the requirement for thin laminae. Then, the three geometrical parameters (η, ξ, γ) are chosen to satisfy Eq. (11) and, finally, the frequency Ω is obtained from Eq. (12). However, the process of imposing a singularity can begin with specifying the frequency first, which is equally valid.

For the numerical computations that follow, we choose $l_y = 120\,\mu\text{m}$ and $l_z = 60^{-1}$, yielding a device thickness of $2\,\mu\text{m}$. Equation (11) defines a constraint that represents the surface shown in Fig. 2. Due to the device periodicity in the x-y plane, we restrict the plotted region using inequality $s/2 - \eta - \gamma \geqslant \gamma$ to avoid including the same device multiple times.

The surface consists of two separate parts that touch at a point where $\gamma = 0$, signifying the merging of two distinct holes into one. This point lies at the intersection of two curves in the (η, ξ)-plane. These curves, visible for $\gamma = 0$ in Fig. 2, obey $\text{sinc}(4\pi\xi) = \text{sinc}(4\pi\eta)$. This is a point which is independent of any chosen device parameters, and we will name the point "SincSync" in recognition of its position at the intersection of two distinct curves associated with the equation $\text{sinc}(4\pi\xi) = \text{sinc}(4\pi\eta)$. The coordinates of this universal point are $\eta = \xi = 0.358$, rounded up to three decimals, Fig. 3. Strict precision is not crucial here, as the BICs are robust to parameter variations, as we will demonstrate later in Sec. VIII. It is important to notice that conditions (11) and (12) are sufficient but not necessary for the existence of BICs. Moving slightly away from this surface, the device still supports BICs, which aligns with the robustness of symmetry-protected BICs at the Γ point.

After selecting (η, ξ, γ) from the surface depicted in Fig. 2, the second constraint (12) determines the frequency required to achieve the desired pattern for the transfer matrix (10). The contour lines of constant frequency are shown in Fig. 3, together with the projection of the surface from Fig. 2 onto the plane (η, ξ). Besides the two curves from $\text{sinc}(4\pi\xi) = \text{sinc}(4\pi\eta)$, a third curve emerges from the downward projection.
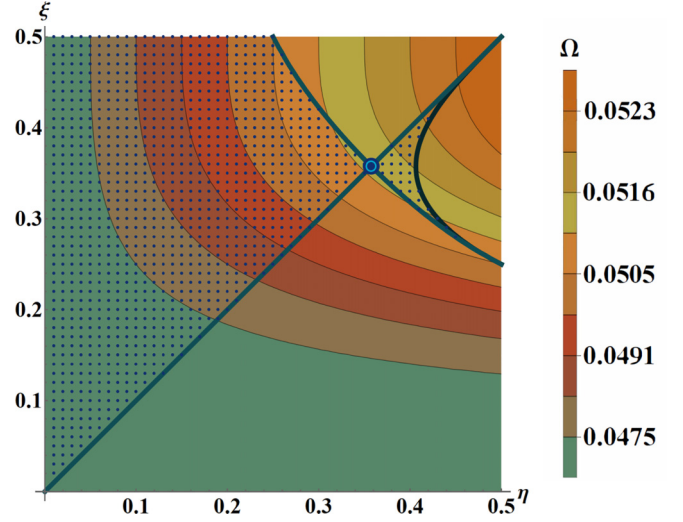

FIG. 3. The dotted region is the projection of the surface from Fig. 2 on the plane (η, ξ). The hyperbolic-like contour plots represent Eq. (12), i.e., they give the constant frequency lines. The legend might have been labeled based on the values of $\eta\xi(1 - \text{sinc}(4\pi\xi))$, from Eq. (12). However, it is instead assigned the frequency Ω, obtained from the same formula for $l_y = 120\,\mu\text{m}$ and a device thickness of $2\,\mu\text{m}$, facilitating a straightforward correlation with the plots from the numerical example.

IV. SYMMETRIC AND ANTISYMMETRIC MATRIX PATTERNS

We will support theoretical result with a numerical example to enhance clarity and to validate the applicability of the theoretical framework. For (η, ξ) values we selected the Sinc-Sync point and, as stated before, $l_y = 120\,\mu\text{m}$ and $l_z = 60^{-1}$. These numerical choices, along with the silicon background permittivity of $\epsilon_B = 11.9$, set the frequency at $\Omega = 0.05126$ using Eq. (12).

The behavior of the transfer matrix of the device around and away from $\Omega = 0.0513$ is illustrated in Fig. 4. A surprising observation is that at lower frequencies, the device
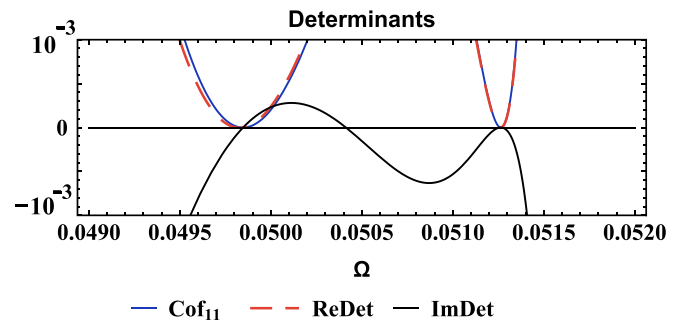

FIG. 4. Determinants. ReDet and ImDet are the real and the imaginary parts of the determinant of the $T^{-,-}$-matrix based on the first five BF modes, $(0, 0)$, $(-1, 0)$, $(1, 0)$, $(0, -1)$, and $(0, 1)$, respectively. Cof_{11} is the cofactor for the element $T_{11}^{-,-}$ of this matrix. A common zero of Eqs. (5) and (6) is present at the designed singularity $\Omega_a = 0.0513$. As a bonus, a second singularity appears at a lower frequency $\Omega_s = 0.0498$. The ReDet and Cof_{11} both have a parabolic shape, taking values above zero.
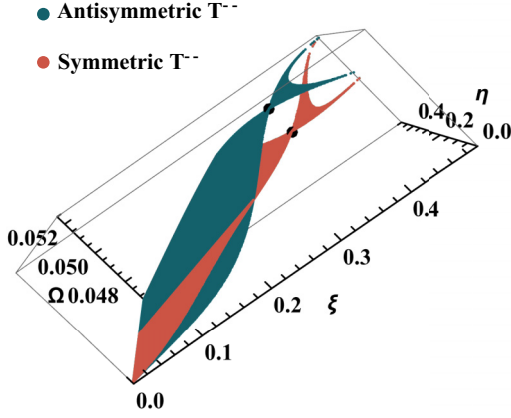
FIG. 5. Separate frequency surfaces correspond to the unitless frequency parameters Ω_a and Ω_s, representing antisymmetric and symmetric patterns, respectively. The intersection of these two surfaces is along the segment $\xi = 1/4$ and $0 < \eta < 1/4$. On this segment $\gamma = (1/8) - (\eta/2)$ and $H = 0$.

exhibits a second frequency worthy of further study. At this lower frequency, for which $\Omega = 0.0498$, the transfer matrix is symmetric. This numerical finding indicates the possibility that both patterns—the symmetric 4×4 submatrix structure

$$\begin{bmatrix} H & H & 0 & 0 \\ H & H & 0 & 0 \\ 0 & 0 & H & H \\ 0 & 0 & H & H \end{bmatrix} \qquad (16)$$

and the antisymmetric one from Eq. (10)—may coexist within the same device. These patterns appear at different frequency values when scanning through the points across the surface depicted in Fig. 2, where the points correspond to different devices.

Indeed, in our quest for a symmetric T^{--} structure (16), we find that while the first condition (11) remains unchanged, the second condition transforms into

$$\eta \xi (1 + \mathrm{sinc}(4\pi\xi)) = \frac{1}{4} \frac{((\epsilon_B - 1)\Omega^2 \Phi_e - 1)^2 - (\Phi_e)^2}{((\epsilon_B - 1)\Omega^2 \Phi_e - 1)^2 - 1}. \qquad (17)$$

Both symmetric and antisymmetric patterns require attention going forward. As the patterns manifest at different frequencies, a natural inquiry arises: how far apart are these two frequencies as we explore all geometrical parameters? Figure 5 captures this frequency difference. A notable distinction exists for the SincSync point compared to many others, as the difference is significantly larger. The comprehensive view of device behavior across various geometries, as illustrated in Fig. 5, can be expanded to encompass other parameters positioned along the vertical axis. Building on this idea, Fig. 6 clarifies the distinction in values taken by matrix element $H = T_{22}^{--}$ for the symmetric and antisymmetric patterns.

Having selected the SincSync device and identified the frequencies of interest, our analysis diverges into two main areas.

First, we establish the basis of the linear space where the relevant modes reside, providing the fundamental set of vectors necessary to discuss the resonances and BIC phenomena.
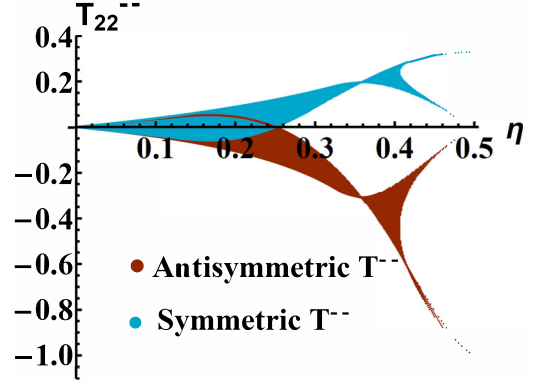

FIG. 6. The values of T_{22}^{--} for the antisymmetric and symmetric patterns. Above each value for η the segment represents all values of T_{22}^{--} for all possible values of ξ.

Second, we move to the complex frequency plane to explore the trajectories of the zeros and poles of the scattering matrix elements as θ and φ vary. The methodology presented here demonstrates versatility—it can be applied across various devices that correspond to points on the surface of Fig. 2.

We base our five-dimensional linear basis on the four eigenvectors of the 4×4 submatrix of the antisymmetric and symmetric patterns, plus the vector W_1 that corresponds to the incoming (0,0) BF mode

$$W_1 = (1, 0, 0, 0, 0), \quad W_2 = (0, 1, 1, 0, 0)/\sqrt{2},$$

$$W_3 = (0, -1, 1, 0, 0)/\sqrt{2}, \quad W_4 = (0, 0, 0, 1, 1)/\sqrt{2},$$

$$W_5 = (0, 0, 0, -1, 1)/\sqrt{2}. \qquad (18)$$

In this W basis, the $T^{-,-}$ matrix (10), which exhibits the antisymmetric pattern, becomes

$$\begin{bmatrix} T_{11} & 0 & -\sqrt{2}T_{12} & 0 & 0 \\ 0 & 0 & 0 & 0 & 0 \\ -\sqrt{2}T_{21} & 0 & 2H & 0 & 0 \\ 0 & 0 & 0 & 0 & 0 \\ 0 & 0 & 0 & 0 & 2H \end{bmatrix}, \qquad (19)$$

whereas for the symmetric pattern (16), the $T^{-,-}$ matrix becomes

$$\begin{bmatrix} T_{11} & 0 & -\sqrt{2}T_{12} & 0 & 0 \\ 0 & 2H & 0 & 0 & 0 \\ -\sqrt{2}T_{21} & 0 & 0 & 0 & 0 \\ 0 & 0 & 0 & 2H & 0 \\ 0 & 0 & 0 & 0 & 0 \end{bmatrix}. \qquad (20)$$

At the antisymmetric pattern frequency Ω_a, Fig. 4, the matrix structure (19) predicts that the device has two BICs corresponding to W_2 and W_4, as observed in the all-zero columns 2 and 4. The association of BICs with zero eigenvalues is also noted in Ref. [25].

At the symmetric pattern frequency, Ω_s, where the structure is given by Eq. (20), W_3 corresponds to a resonance, while W_5 corresponds to a BIC, evident from columns 3 and 5. To further confirm that W_3 corresponds to a resonance at the lower frequency Ω_s, we examine the 2×2 matrix coupling W_1 and W_3 in Eq. (20). Its elements exhibit the resonant

trait: in this particular W basis, T_{33} equals zero, while the remaining three elements do not [26]. The eigenvectors from Eq. (18) exhibit symmetric and antisymmetric combinations of BF modes, arising from the transfer matrix patterns (10) and (16).

The distinction between the resonance and the BIC, along with further clarification of their meanings, is fundamentally related to the zeros and poles of the scattering matrix elements, as will be covered in Sec. VII.

In the forthcoming sections, we delve into these predictions. Of particular interest is the conversion of a BIC into a quasi-BIC, necessitating the transition from $\theta = 0$ to $\theta \neq 0$; simultaneously, some quasi-BICs require $\varphi \neq 0$.

V. ANALYSIS OF THE TWO BICs AT THE ANTISYMMETRIC PATTERN FREQUENCY Ω_a.

To investigate the behavior of the SincSync device away from $\theta = 0$, $\varphi = 0$ and within frequency regions centered on $\Omega_{a/s}$, we employ a series expansion of the transfer matrix elements expressed in the BF basis. It is not obvious upfront if a first order in (θ, φ) works, so we went with a second order expansion to hopefully capture the behavior of the BICs

$$T^{-,-} = T_{000} + T_{010}\,\theta + T_{001}\,\varphi + T_{020}\,\theta^2$$
$$+ T_{011}\,\theta\varphi + T_{002}\,\varphi^2 + T_{100}\,\Delta + \cdots. \quad (21)$$

Here Δ is a small variation in frequency away either from the antisymmetric $\Omega_a = 0.0513$ or symmetric frequency

$\Omega_s = 0.0498$:

$$\Omega = \Omega_{s/a} + \Delta_{s/a}. \quad (22)$$

This expansion was carried out in both symbolic and numerical format. As a result, the determinant of $T^{-,-}$ and all its cofactors become polynomials of at least fourth order in the frequency parameter $\Delta_{s/a}$. Given that the observed behavior resembles a parabolic shape in Fig. 4, we require only second-order rational functions in $\Delta_{s/a}$ for each scattering matrix element. In other words, two zeros and two poles for each of the scattering matrix elements will be both necessary and sufficient to accurately represent the behavior of either the pair of BICs at Ω_a or the pair consisting of a resonance and a BIC at Ω_s. This conclusion explains why stopping at the first order in Δ in Eq. (21) is sufficient.

We identify the poles and zeros of the scattering matrix elements as perturbations around specific frequencies where the diagonal elements of the transfer matrix vanish. This approach offers two advantages. First, we can treat the frequency region containing the two BICs independently from the resonance and its accompanying BIC. Second, this separation allows us to work with smaller, 3×3 submatrices. One submatrix deals with the coupling of vectors W_1, W_2, and W_4 in relation to the two BICs, while the other concentrates on the coupling of W_1, W_3, and W_5 associated with the resonance and its BIC.

We start by selecting the 3×3 submatrix that couples W_1, W_2, and W_4, i.e., the coupling between the incoming wave and the two BICs, where $\Delta_a = \Omega - \Omega_a$. The result is the matrix $T^{-,-}_{W_1 W_2 W_4}$ from Eq. (23) expressed in the W basis:

$$T^{-,-}_{W_1 W_2 W_4} = \begin{bmatrix} A_{11} + \Delta_a\beta_{11} + \theta^2\mu_{11} & \sqrt{2}\theta B_{12} & \sqrt{2}\theta B_{14} \\ \sqrt{2}\theta B_{21} & \Delta_a\beta_{22} + \Delta_a\beta_{32} + \theta^2\mu_{22} + \theta^2\mu_{32} & 2\theta^2\mu_{24} \\ \sqrt{2}\theta B_{41} & 2\theta^2\mu_{42} & \Delta_a\beta_{22} + \Delta_a\beta_{32} + \theta^2\mu_{44} + \theta^2\mu_{54} \end{bmatrix}. \quad (23)$$

The meanings of the symbols can be deduced from the accompanying parameters. For instance, the Greek symbol μ represents the matrix elements of T_{020}, reflecting the second-order expansion in θ as shown in Eq. (21). The scattering matrix elements in Eqs. (24)–(26) are obtained by taking the inverse of $T^{-,-}_{W_1 W_2 W_4}$, with the index (min, max) implied, whereas in Eq. (2) it is explicit. The poles of the scattering matrix elements, p_1 and p_2 are complex numbers, a property inherited from the elements in the first row and first column of Eq. (23), which are complex numbers as they exhibit the coupling into the propagative BF mode (0,0).

In contrast, the zeros of $S_{W_1 W_1}$, z_1 from Eq. (27), and z_2 from Eq. (28) are located on the real axis because they are based on transfer matrix elements that couple evanescent modes within themselves, which are real numbers in lossless dielectric devices.

The symbolic formulas for the poles are presented in Appendix.

$$S_{W_1 W_1} = \frac{1}{A_{11}} \frac{\Delta_a - z_1}{\underbrace{\Delta_a - p_1}_{\text{quasi-BIC}_1}} \frac{\Delta_a - z_2}{\underbrace{\Delta_a - p_2}_{\text{quasi-BIC}_2}}, \quad (24)$$

$$S_{W_2 W_1} = \theta \frac{-\sqrt{2}\,B_{21}}{A_{11}(\beta_{22} + \beta_{32})} \frac{\Delta_a - z_{W_2}}{(\Delta_a - p_1)(\Delta_a - p_2)}, \quad (25)$$

$$S_{W_4 W_1} = \theta \frac{-\sqrt{2}\,B_{41}}{A_{11}(\beta_{22} + \beta_{32})} \frac{\Delta_a - z_{W_4}}{(\Delta_a - p_1)(\Delta_a - p_2)}, \quad (26)$$

$$z_1 = -\frac{\mu_{2,2} + \mu_{3,2}}{\beta_{2,2} + \beta_{3,2}}\theta^2 - \frac{4\mu_{2,4}\mu_{4,2}}{(\beta_{2,2} + \beta_{3,2})(\mu_{2,2} + \mu_{3,2} - \mu_{4,4} - \mu_{5,4})}\theta^2, \quad (27)$$

$$z_2 = -\frac{\mu_{44} + \mu_{54}}{\beta_{22} + \beta_{32}}\theta^2 + \frac{4\mu_{24}\mu_{42}}{(\beta_{22} + \beta_{32})(\mu_{22} + \mu_{32} - \mu_{44} - \mu_{54})}\theta^2. \quad (28)$$
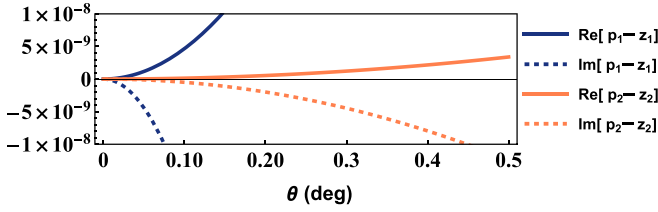
FIG. 7. The quadratic evolution of the (pole, zero) pair with respect to θ is depicted for the antisymmetric case. The plotted pole-zero difference, based on our numerical example, illustrates the Q factor diverging to infinity as θ approaches zero.

The format of these matrix elements is that of a second-order rational function, which occurs in the field of circuits and systems [27]. Additionally they are utilized for fitting experimental data in the field of optics [28,29].

There are certain aspects of this result that are important to discuss. One aspect pertains to the structure of $S_{W_1W_1}$ when viewed as a product of two linear fractional functions, also known as Möbius or bilinear transformations, each representing a Fano line shape [30]. This contrasts with the more common approach of considering the numerator and denominator separately, as second order polynomials [27]. Viewing $S_{W_1W_1}$ as a product of Fano line shapes brings us closer to the Weierstrass factorization for an entire function, which is employed in scattering problems [31–33]. The study of BICs is facilitated by examining each linear fractional function, where its zeros and poles converge, as $\theta \to 0$, to a common point on the real axis, as shown for the numerical example in Fig. 7. The implications of these results will be further explored in Sec. VI. Until then, we will go over the derivation of these scattering matrix elements.

In contrast to z_1 and z_2 of $S_{W_1W_1}$, which are real numbers in this approximation, the zeros of $S_{W_2W_1}$ and $S_{W_4W_1}$ have an imaginary component introduced by the coupling with the propagative mode through B_{21} and B_{41}. These zeros, z_{W2} and z_{W4}, are exact and derived from the cofactors of Eq. (23):

$$z_{W2} = -\theta^2 \frac{\mu_{44} + \mu_{54}}{\beta_{22} + \beta_{32}} + \theta^2 \frac{2B_{41}\mu_{24}}{B_{21}(\beta_{22} + \beta_{32})}, \quad (29)$$

$$z_{W4} = -\theta^2 \frac{\mu_{22} + \mu_{32}}{\beta_{22} + \beta_{32}} + \theta^2 \frac{2B_{21}\mu_{42}}{B_{41}(\beta_{22} + \beta_{32})}. \quad (30)$$

A resonance is usually described solely by a single pole, where the imaginary part characterizes the energy dissipation or decay rate of the resonant mode, making the Q factor inversely proportional to it. However, in certain resonances, such as in this case, both a zero and a pole are required for an accurate description, with the zero becoming as significant as the pole. Since the zeros of the Fano line shapes describing the quasi-BICs are located on the real frequency axis in the small-angle approximation [as given in Eqs. (27) and (28)], it is necessary to determine the imaginary parts of the poles to fully describe the Fano line shapes.

The imaginary parts of both poles are determined as perturbations of the real roots, as shown in Eqs. (31) and (32).

The unknowns X_1 and X_2 are determined such that the lowest-order term in the expansion of the determinant of Eq. (23) becomes θ^4.

$$p_1 = -\theta^2 \frac{\mu_{2,2} + \mu_{3,2}}{\beta_{2,2} + \beta_{3,2}} + 2\theta^2 X_1, \quad (31)$$

$$p_2 = -\theta^2 \frac{\mu_{4,4} + \mu_{5,4}}{\beta_{2,2} + \beta_{3,2}} + 2\theta^2 X_2. \quad (32)$$

In the numerical example, the imaginary parts are three orders of magnitude smaller than their real parts. The same procedure is used to find the real zeros z_1 and z_2 from the cofactor of Eq. (23).

The Q factor of both poles contains a term proportional to Ω_a/θ^2, indicating that it tends toward infinity as θ decreases.

Apart from the Q factors associated with the poles, other aspects are also important. The poles and zeros for both Fano lines from Eq. (24), which describe the quasi-BICs, evolve with the square of the angle θ. At $\theta = 0$, each pole collides with its corresponding zero, marking the transition of the quasi-BIC into a true BIC. This evolution is illustrated in Fig. 7, based on the numerical example.

Because $W_1 = BF_1 = (1, 0, 0, 0, 0)$, we have $S_{W_1W_1} = S_{11}|_{\text{base-BF}}$, which is directly visible in the numerical simulations, as shown in Figs. 12(a)–12(c). Additionally, note that we are working not only in the W basis but also in a changed basis performed by the diagonal matrix U, Eq. (3). Keeping the W basis and removing the U-dependent basis, we need to multiply $S_{W_2W_1}$ and $S_{W_4W_1}$ by $\sin(\theta)$ while $S_{W_1W_1}$ remains unchanged. This is important for comparing with the full-wave numerical simulations [20]. To avoid any confusion, we emphasize that we will continue to use the new basis Eq. (3) in what follows.

VI. QUASI-BICS AND NONCOMMUTING LIMITS

To observe a quasi-BIC state brought in by a small θ, we examine the output state at $z_{\min}$ when the propagating plane wave W_1 reaches the device at $z_{\max}$,

$$\text{Out}_{\min} = S_{W_1W_1}W_1 + S_{W_2W_1}W_2 + S_{W_4W_1}W_4. \quad (33)$$

We find that for $\theta = 0$, $S_{W_1W_1} \neq 0$ but $S_{W_2W_1} = S_{W_4W_1} = 0$, due to the presence of θ as a standalone factor in Eqs. (25) and (26). Additionally, at $\theta = 0$ and $\Delta_a = 0$, we notice L'Hôpital's rule, resulting in $S_{W_1W_1} = 1/A_{11}$. The output state becomes a pure propagating wave

$$\text{Out}_{\min} = (A_{11})^{-1} W_1, \quad (34)$$

bearing no visible trace of the evanescent waves W_2 and W_4 that characterize the BICs.

The existence of the quasi-BICs is demonstrated by the ability to eliminate the propagating mode W_1 at $z_{\min}$ when $S_{W_1W_1} = 0$. The elimination—occurring at two frequencies $\Delta_a = z_1$ or z_2 [Eqs. (27) or (28)], if we stay in the frequency region around Δ_a—results in the output field being a superposition of only the evanescent modes W_2 and W_4.

This quasi-BIC state warrants an exploration into the limit $\theta \to 0$. An important feature of this limit is that it imposes a constraint between Δ_a and θ, namely the parabolic constrain $\Delta_a = z_1$ (with z_1 as an example). This equation defines a specific path in the (θ, Δ_a) plane on which the limit is taken.
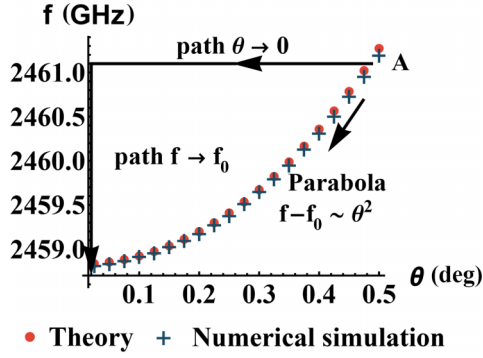
FIG. 8. Following two distinct paths from point A toward the origin, we obtain different results, thereby justifying the noncommuting limits in Eq. (35). The values of the pair (θ, f) that result in zero transmission $S_{W_1 W_1}$ form a parabola. The set of frequencies corresponds to one of the two quasi-BICs located in the vicinity of Ω_a. The quasi-BIC turns into a BIC for $\theta = 0$ at $f_0 = 2458.8$ GHz. This parabola, as predicted by the theory for the chosen numerical values $l_y = 120\,\mu m$ and a device thickness of $l_z = 2\,\mu m$, is $f = 2458.8 + 9.5\,\theta^2$ in GHz. The relation between the frequency f and the unitless frequency parameter Ω is $\Omega = (l_z/2)(2\pi f/v_0)$, where v_0 is the speed of light in vacuum and l_z, in μm, the thickness of the device from Fig. 1. As also reported in Ref. [17], a systematic shift exists between the theoretical and simulated frequencies. Here, all the theoretical frequencies are 12.87 GHz less than the simulated ones. This amounts to a 0.52% error for this frequency band. To enhance precision, we used a 9×9 transfer matrix to compute the parabola along which the device is entirely opaque. The added four BF modes are $(\pm 1, \pm 1)$. The influence of higher modes is discussed in Sec. VIII.

Taken on a different path, the limit is different, which is actually a signature of the singularity introduced into the transfer matrix.

A practical numerical approach we implemented using 3D electromagnetic simulation software [20] involves tracking the path-dependent effect by examining the limit behavior of the transmission scattering element, $S_{W_1 W_1} = S_{11}$, as it approaches the point $(\theta = 0, \Delta_a = 0)$ along the two paths shown in Fig. 8.

The constant value of $S_{W_1 W_1} = 0$ along the parabola ensures a limit of zero, meaning complete opacity.

However, if we first set $\theta = 0$ and then follow the vertical frequency axis until Δ_a reaches 0, we end up with $S_{W_1 W_1} = A_{11}^{-1} = 0.88 + 0.39i$. This value indicates that the device is almost transparent.

The typical switching effect from opacity to transparency in the presence of a BIC can be summarized as

$$0 = \lim_{\text{parabola}} S_{W_1 W_1} \neq \lim_{\Delta_a \to 0} \lim_{\theta \to 0} S_{W_1 W_1} = A_{11}^{-1}. \tag{35}$$

VII. ANALYSIS OF THE RESONANCE AND ITS ACCOMPANYING BIC AT THE SYMMETRIC PATTERN FREQUENCY Ω_s

The resonance and its accompanying BIC are located around the frequency Ω_s that corresponds to the symmetric pattern of the transfer matrix. Resonance typically suggests a pole near the real axis in the frequency complex plane. However, the scattering matrix elements in the present case reveal a Fano resonance involving both a pole and a zero.

To analyze the resonance W_3 and its associated BIC W_5, we consider the 3×3 matrix describing the coupling between the incoming mode W_1 and the pair (W_3, W_5). Near Ω_s, the transfer matrix in the subspace spanned by (W_1, W_3, W_5) takes the form shown in Eq. (36):

$$T_{W_1^- W_3^- W_5}^- = \begin{bmatrix} a_{11} + \Delta_s \beta_{11} + \theta^2 \mu_{11} & -\sqrt{2}(a_{12} + \Delta_s \beta_{12} + \theta^2 \mu_{12} + \varphi^2 \tau_{12}) & -\sqrt{2}\varphi v_{14} \\ -\sqrt{2}(a_{21} + \Delta_s \beta_{21} + \theta^2 \mu_{21} + \varphi^2 \tau_{21}) & \Delta_s \beta_{22} - \Delta_s \beta_{32} + \theta^2 \mu_{22} - \theta^2 \mu_{32} & 0 \\ -\sqrt{2}\varphi v_{41} & 0 & \Delta_s \beta_{22} - \Delta_s \beta_{32} + \theta^2 \mu_{44} - \theta^2 \mu_{54} \end{bmatrix}. \tag{36}$$

The following results, obtained from Eq. (36), pertain to the scattering matrix elements that couple W_1 at $z_{\max}$ into W_3 and W_5 at $z_{\min}$:

$$S_{W_3 W_1} = \frac{a_{21}\sqrt{2}}{-2a_{21}\beta_{12} - 2a_{12}\beta_{21} + a_{11}(\beta_{22} - \beta_{32})} \frac{\Delta_s - z_{W3}}{(\Delta_s - p_{W3})(\Delta_s - p_{W5})}, \tag{37}$$

$$S_{W_5 W_1} = \varphi \frac{v_{41}\sqrt{2}}{-2a_{21}\beta_{12} - 2a_{12}\beta_{21} + a_{11}(\beta_{22} - \beta_{32})} \frac{\Delta_s - z_{W5}}{(\Delta_s - p_{W3})(\Delta_s - p_{W5})}. \tag{38}$$

The transmission of the incoming propagative mode is

$$S_{W_1 W_1} = \frac{\beta_{22} - \beta_{32}}{-2a_{21}\beta_{12} - 2a_{12}\beta_{21} + a_{11}(\beta_{22} - \beta_{32})} \underbrace{\frac{\Delta_s - z_{W5}}{\Delta_s - p_{W3}}}_{\text{resonance}} \underbrace{\frac{\Delta_s - z_{W3}}{\Delta_s - p_{W5}}}_{\text{quasi-BIC}}. \tag{39}$$

Note that, contrary to Eq. (23), φ is part of the matrix $T_{W_1^- W_3^- W_5}^-$. The meaning of the symbols in Eq. (36), as in Eq. (23), comes from the series expansion (21).

For $\varphi = 0$, the matrix becomes block-diagonal, with W_5 decoupled from W_1 and W_3. Thus, transforming W_5 from a BIC to a quasi-BIC requires setting $\varphi \neq 0$. A comparable

dependence on parameter values, specifically the need for a nonzero θ, will also emerge later when examining the zeros and poles of the scattering matrix elements.

Resolving the zeros and poles related to the resonance entails a procedure distinct from merely solving for the root of the diagonal element (W_3, W_3), Eq. (36). This distinction arises from our earlier discussion of the resonance at Ω_s and $(\theta = 0, \varphi = 0)$, which involved the 2×2 submatrix of the matrix (20) that couples W_1 and W_3. Here, for the quasi-BIC regime $(\theta \neq 0, \varphi \neq 0)$, the 2×2 matrix that couples W_1 and W_3 in $T_{W_1 W_3 W_5}^{-;-}$ is

$$\begin{bmatrix} a_{11} & -\sqrt{2}a_{12} \\ -\sqrt{2}a_{21} & \Delta_s \beta_{22} - \Delta_s \beta_{32} + \theta^2 \mu_{22} - \theta^2 \mu_{32} \end{bmatrix}. \quad (40)$$

Notice that we neglect the small numbers Δ_s, θ and φ with respect to a_{11}, a_{12} and a_{21}. By setting the determinant of this matrix to zero and keeping the zero-order approximation in θ, the root is obtained as

$$\mathrm{r}_{W3\mathrm{complex}} = \frac{2\, a_{12} a_{21}}{a_{11}(\beta_{22} - \beta_{32})}. \quad (41)$$

This is a complex number given that the numbers a_{mn}, $m, n = 1, 2$ are complex, as they relate to the incoming propagative BF mode $(0,0)$. Two additional roots from the diagonal elements of Eq. (36) associated with the resonance W_3 and the BIC W_5 are located on the real frequency axis:

$$\mathrm{r}_{W3\mathrm{real}} = -\theta^2 \frac{\mu_{22} - \mu_{32}}{\beta_{22} - \beta_{32}}, \quad (42)$$

$$\mathrm{r}_{W5} = -\theta^2 \frac{\mu_{44} - \mu_{54}}{\beta_{22} - \beta_{32}}. \quad (43)$$

From these three roots, we construct the zeros and poles of the scattering matrix using a series approximation:

$$z_{W3} = \mathrm{r}_{W5} = -\theta^2 \frac{\mu_{44} - \mu_{54}}{\beta_{22} - \beta_{32}}, \quad (44)$$

$$p_{W5} = -\theta^2 \frac{\mu_{44} - \mu_{54}}{\beta_{22} - \beta_{32}} + \theta^2 \varphi^2 (X + \theta^2 Y + \varphi^2 Z), \quad (45)$$

$$X = -\frac{(\mu_{2,2} - \mu_{3,2} - \mu_{4,4} + \mu_{5,4})\nu_{1,4}\nu_{4,1}}{(\beta_{2,2} - \beta_{3,2})a_{1,2}a_{2,1}}. \quad (46)$$

Apparently, the expansion up to X would be sufficient for the pole to display its imaginary part, given that $\nu_{1,4}$, $\nu_{4,1}$, $a_{1,2}$, and $a_{2,1}$ are each complex numbers, by virtue of their coupling with the propagative mode W_1.

However, the reason we cannot stop at X and must continue to find the next approximation order, given by Y and Z in Eq. (45), is that for $s = 1$, the following ratios of complex numbers are, in fact, real

$$\frac{\nu_{1,4}}{a_{1,2}} = \frac{\nu_{4,1}}{a_{2,1}} = \frac{\mathrm{sinc}(2\pi\xi)}{\cos(\pi(2\gamma + \eta))\mathrm{sinc}(\pi\eta)}. \quad (47)$$

This means that the imaginary part of the p_{W5} needs to come out from series expansion beyond $\theta^2 \varphi^2$.

Studying these matrix elements clarifies the concept of BIC at Ω_s, linking the null subspace of the transfer matrix to the arrangement of zeros and poles in the complex frequency plane.

For $\varphi = 0$, we observe that the numerator simplifies in S_{W3W1} (37) even when $\theta \neq 0$, resulting in the elimination
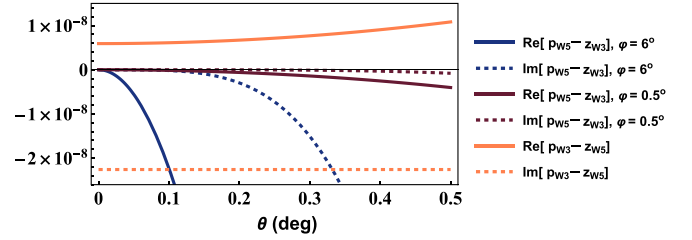

FIG. 9. For the resonance-BIC pair, the evolution of the difference between the pole and zero depends on both θ and φ. At $\varphi = 0$, the quasi-BIC cannot be excited by a positive value of θ.

of the BIC from this scattering matrix element. However, in S_{W5W1} (38), such simplification does not occur; instead, the presence of φ in the numerator renders the entire scattering matrix element null at $\varphi = 0$. We conclude that the BIC can transition into a quasi BIC only in the presence of nonzero θ and φ. The dependence on φ was also inferred directly from the transfer matrix (36), which turns block-diagonal for $\varphi = 0$.

The signature of the quasi-BIC in S_{W1W1}, Eq. (39), springs from the term $(\Delta_s - z_{W3})/(\Delta_s - p_{W5})$, which is visible in transmission as a deep, narrow notch as long as $\theta \approx 0$ and $\varphi \approx 0$, but not zero, as will be discussed in Sec. VIII.

Significantly, the quasi-BIC term in Eq. (39) simplifies to 1 when $\theta = 0$, yet the factor $\Delta_s - z_{W5}$ persists in the numerator due to the presence of the complex pole p_{W3} in the denominator. The occurrence of this factor in the numerator of S_{W1W1} is reflected in transmission dropping to zero observed at $\theta = 0$ in both theoretical models and numerical simulations, as shown in Sec. VIII. The identical phenomenon is absent in the case of two BICs around Ω_a, as the quadratic Δ_a in the numerator simplifies with a quadratic Δ_a in the denominator, Eq. (24). The complex pole p_{W3} at $\theta = 0$, $\varphi = 0$ is distinctly observable in S_{W3W1}, given that is is very close to the real frequency axis. The disparity in the visibility of this complex pole in S_{W3W1} but not in S_{W5W1} at $\theta = 0$, $\varphi = 0$, further strengthens our association of the term resonance with the mode W_3, stemmed from the transfer matrix in Sec. III.

This discussion is supported by the numerical example in Fig. 9, illustrating the trajectory of the difference between poles and zeros as the quasi-BIC transitions into a BIC, along with the characteristics of the Fano resonance. The behavior as φ approaches zero is also evident.

The transition from a quasi-BIC to a BIC can furthermore be interpreted through an analogy with an electrostatic model Fig. 10, as shown in Ref. [34].

As φ goes to zero, the rightmost charges $+1$ and -1 come closer to each other, annihilating at $\varphi = 0$. This annihilation marks the transition of the quasi-BIC into a BIC. The zero from the left is not annihilated even if both angles become zero. This is responsible for the resonance dip in the transmission S_{W1W1}, as described in Eq. (39).

The correction in $\theta^2 \varphi^2$ from Eq. (45) to the quasi-BIC's pole is not shown in Fig. 10, being too small to be visible. The parameter $\Delta = \Delta_s$ was scaled, and θ and φ were chosen to facilitate the visualization of the singular points, given that these adjustments do not influence the values of the charges.
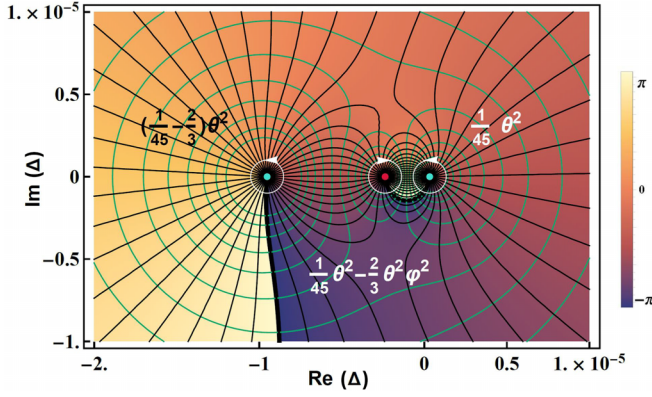
FIG. 10. The electrostatic model for resonance and its quasi-BIC. The angle-dependent zeros z_{W3} and z_{W5}, along with the pole p_{W5} of $S_{W_1 W_1}$ from Eq. (39), are displayed within the plotted region, while the second pole p_{W3} lies outside this range. The plot shows contour lines for the complex electrostatic potential $\ln(S_{W_1 W_1})$. The real part of the complex potential is in emerald green, whereas the imaginary part in black. At each three singular point a charged line, perpendicular to the plane, is located. The zeros, marked with green disks have a charge of $+1$, whereas the pole, marked red, has a charge of -1. The real-axis positions of these three singularities are determined from the numerical example and are expressed as functions of the angles θ and φ, with the approximations provided as rational numbers for clarity.

FIG. 11. On the vertical axis, on a logarithmic scale, D represents a pair formed by the determinant of $T^{-,-}$, plotted as a continuous line, and the cofactor of its $T_{11}^{-,-}$ matrix element, plotted as a dashed line. Three pairs of curves are represented, corresponding to 5, 9, and 25 modes. The curves belonging to the same pair superimpose, showing that they indeed share common zeros at $\theta = 0$ and $\varphi = 0$. The region on the right side of the frequency axis belongs to the antisymmetric pattern where the two BICs are located. For the five-dimensional case, at $\theta = 0$ and $\varphi = 0$, these two BICs coincide, as Fig. 4 also shows. They become distinct as quasi-BICs. However, increasing the number of modes beyond five causes the BICs to be located, at $\theta = 0$ and $\varphi = 0$, at distinct frequencies, although close to each other. The region on the left side of the frequency axis belongs to the symmetric pattern where the resonance and its BIC are located. The BIC that accompanies the resonance is visible through the rate of decrease being larger for the cofactor than for the determinant around the roots.

VIII. IMPACT OF HIGHER BLOCH-FLOQUET MODES AND COMPARISON TO NUMERICAL SIMULATIONS

With the device's behavior well-characterized within the five-dimensional subspace of modes, it becomes essential to determine whether these findings hold in an expanded dimensional framework. To this end, we will apply our analysis to the selected numerical example.

Figure 11 demonstrates how expanding the subspace dimension confirms both the existence and frequency position of the BICs and the resonance. At $\theta = 0$ and $\varphi = 0$, the BICs are not discernible in S_{11}. However, our approach allows for independent plotting of the numerator and denominator of S_{11}, providing full visibility of the poles and zeros, even when they coincide. To enhance visibility in the presence of higher modes, Fig. 11 employs a logarithmic scale on the vertical axis, in contrast to the linear scale used in Fig. 4.

The right side of the frequency axis, in the vicinity of $\Omega = \Omega_a$, corresponds to the antisymmetric pattern. Here, for 5 modes, both the determinant and the cofactor have a real double root at Δ_a, as we discuss in relation to Fig. 4. This double root property does not survive in the presence of a larger number of modes. The double root splits into two simple real roots, visible for 9 and 25 modes. In logarithmic scale, a double root can be distinguished from a simple root by the more rapid descent of its notch.

Two BICs are still present in the frequency region of the antisymmetric pattern, but they are positioned at different frequencies, which become stable by 25 modes at $\Omega_{a1} = 0.05126$ and $\Omega_{a2} = 0.05088$.

The left side of the frequency region in Fig. 11 is the location of the resonance and its accompanying BIC. The
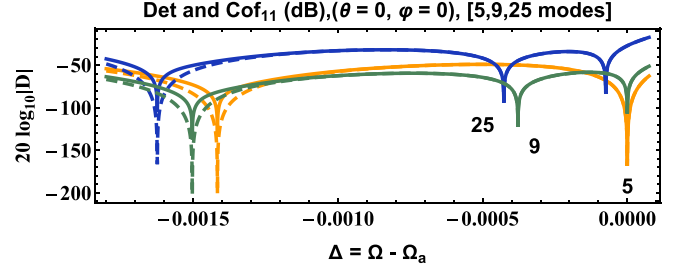
cofactor has a real double root in five dimensions, a property that is maintained as the number of modes increases. The determinant has a simple real root that coincides with the double root of the cofactor, causing it to decrease more gradually than the cofactor's notch. This root shifts to the lower frequency as the number of modes increases, eventually reaching the value $\Omega_s = 0.04976$ by 25 modes Fig. 11. The accompanying BIC is not separately visible because, for $\theta = 0$ and $\varphi = 0$, it becomes the second of the double roots of the cofactor.

The three panels of Fig. 12, each obtained using 25 modes, demonstrate both theoretically and through full-wave numerical simulations [20] that the transmission characteristics of the quasi-BICs, initially identified with five modes, remain robust despite the inclusion of a large number of BF modes.

Figure 12(a) shows the theoretical results plotted in blue. On the left, the two dips in blue correspond to the resonance $f_{\text{Resonance}} = 2352.44$ GHz and its accompanying quasi-BIC $f_{\text{BIC of Resonance}} = 2368.66$ GHz, both associated with the symmetric pattern of the transfer matrix. On the right, for the antisymmetric pattern, also in blue, the two quasi-BICs appear at $f_{\text{BIC}_{1a}} = 2431.64$ GHz and $f_{\text{BIC}_{2a}} = 2452.16$ GHz.

The numerical simulations are plotted in red, except for the quasi-BIC associated with the resonance, which is plotted in cyan. All numerical simulations are shifted to slightly higher frequencies. To superpose them on the theoretical dips, a downward shift of 20 GHz was needed for quasi-BIC$_{1a}$, whereas for the rest, it was 17 GHz, resulting in an error of about 0.8% in this frequency band.

The numerical simulation dedicated to the quasi-BIC associated with the resonance was difficult to perform because its dip covers a range of less than 10 MHz. This presented a clear advantage for the theory, as setting up a numerical simulation
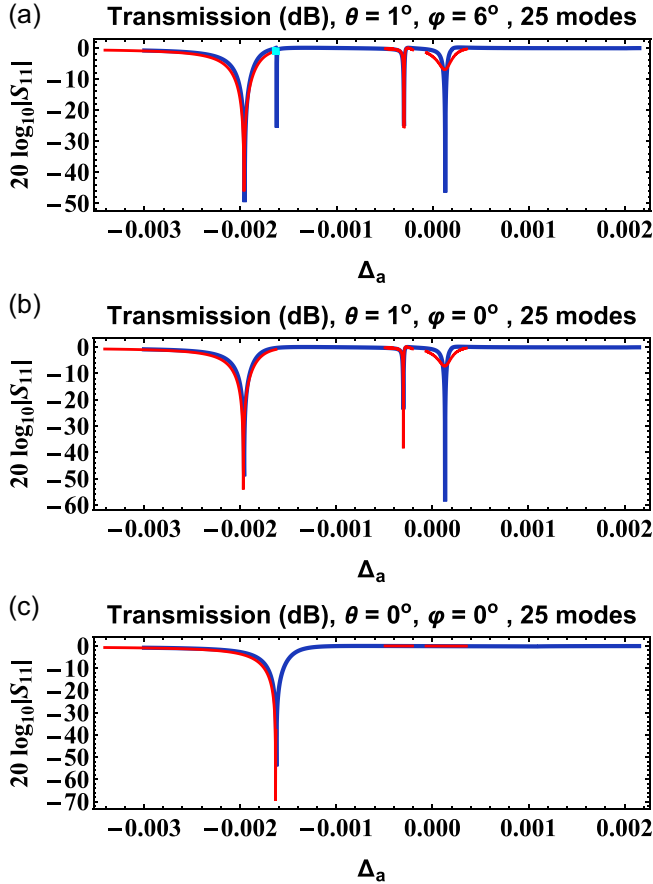
FIG. 12. The quasi-BICs convert into BICs as the angles are switched off. This property, designed using five modes, survives in the presence of a large number of Bloch-Floquet modes and is confirmed by full-wave numerical simulations. (a) The theoretical results are plotted in blue with respect to $\Delta_a = \Omega - \Omega_a$. The numerical simulations are plotted in red, except for the quasi-BIC at resonance, which appears in cyan. This resonance is extremely narrow, making it challenging to resolve in the full-wave numerical simulations. All four dips in transmission are present for $\theta \neq 0$ and $\varphi \neq 0$. Their order, from left to right, is as follows: resonance, quasi-BIC of the resonance, quasi-BIC$_{1a}$, and quasi-BIC$_{2a}$. (b) The quasi-BIC that accompanies the resonance becomes a BIC for $\varphi = 0$, and is thus absent in transmission. The two quasi-BICs associated with the anti-symmetric pattern are not affected by switching off φ. (c) For $\theta = 0$ and $\varphi = 0$, all three quasi-BICs become three distinct BICs. The resonance remains visible.

without it would have been highly impractical. The numerical simulation plotted in cyan appears more like a dot than a dip because it lacks the vertical range seen in the corresponding theoretical plot, which is shown in blue.

Figures 12(b) and 12(c) confirm that the quasi-BICs convert into BICs when one or both of the angles are set to zero, even in the presence of a large number of BF modes.

A separate line of inquiry concerns the precision of the SincSync point defined in Fig. 3, which underpins our numerical simulations. Specifically, we demonstrate by full-wave numerical simulations that fabrication deviations of $\pm 1\%$ in the dimensions of ξ and η from this point do not eliminate the BICs, preserving their properties as shown in Fig. 13.
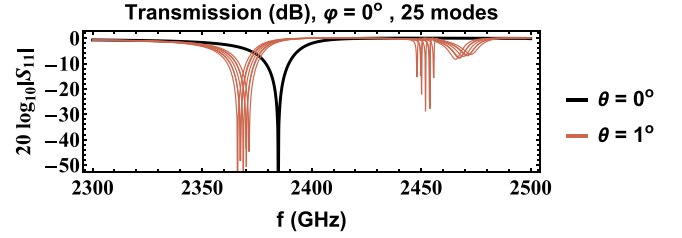

FIG. 13. The figure, obtained through full-wave numerical simulation, shows the frequency positions of the resonance and the pairs of quasi-BICs for $\pm 1\%$ variations in the hole dimensions $\eta = \xi = 0.358$. The BIC associated with the resonance is too narrow to appear within the displayed frequency range.

Finally, using full-wave simulations [20], we present in Fig. 14 the field patterns for the two quasi-BICs associated with the antisymmetric case. Figures 14(b*) and 14(B*) reveal vortices in the electric field, while Figs. 14(a*) and 14(A*) exhibit vortices in the magnetic field. In contrast, Figs. 14(a), 14(A), 14(b), and 14(B) highlight the C_4 symmetry.

IX. CONCLUSION

In this paper, we demonstrated that the singularity of the transfer matrix is advantageous for generating BICs. At the singular point, the transfer matrix becomes noninvertible, leading to an undefined scattering matrix. This singularity is directly linked to the BIC states, which correspond to the null space of the transfer matrix. Consequently, the singularity imposes constraints on geometry, permittivity, and frequency, confining them to specific surfaces in parameter space. These surfaces can be effectively described by two simple and practical design Eqs. (11) and (12).

The photonic slab devices supporting BICs were designed using a transfer matrix constructed from five Bloch-Floquet modes, with one propagating mode and four evanescent modes. These evanescent modes contribute to the spatial localization property of BICs, with the BIC state emerging as a linear combination of the evanescent modes, while the BF (0,0) mode serves as the sole radiative component. After analyzing the device's behavior in a 5-dimensional subspace, we extended our analysis to a 25-dimensional subspace, confirming that the properties of BICs remain intact. A key advantage of our approach, compared to full-wave numerical simulations, is the ability to separate the numerator and denominator of the scattering matrix elements, providing clear visibility of poles and zeros, even when they coincide. This capability allows us to accurately track system behavior as the dimensional subspace increases, ensuring the robustness of our theoretical predictions across different configurations.

The transition from quasi-BICs to BICs is demonstrated through the path-dependent behavior of the scattering matrix in the angle-frequency plane. Theory, backed by numerical simulations, reveals a noncommuting limit, where the device transitions from opacity to near transparency depending on the approach path. This highlights the distinct properties of quasi-BICs and their practical implications for controlling wave transmission.
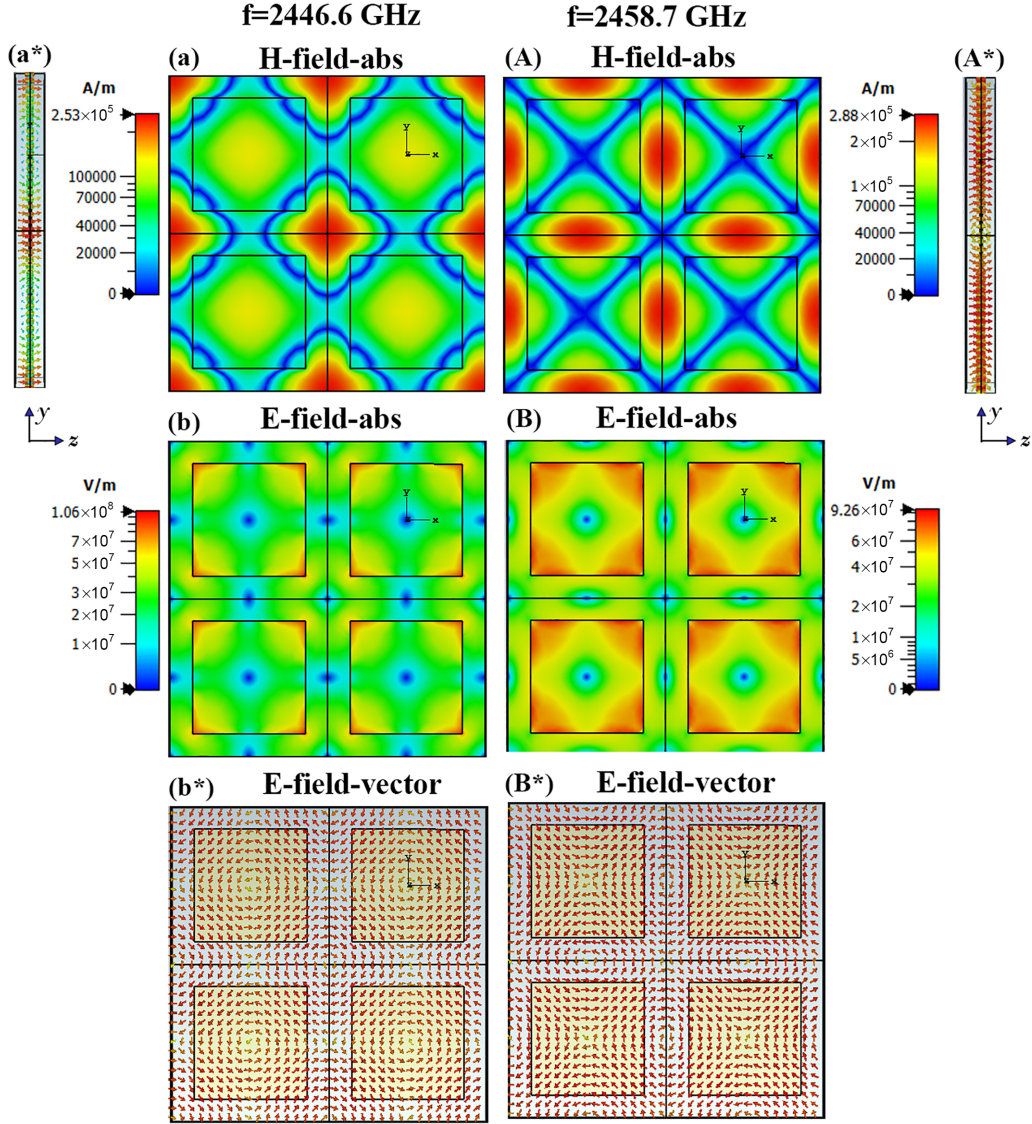
FIG. 14. Full-wave plots for the SincSync geometrical parameters at $(\theta = 0.05°, \varphi = 0°)$, based on 40 BF modes—comprising 20 S-polarized and 20 P-polarized modes—for the two BICs associated with the antisymmetric pattern. The full-wave plots are based on $\Re[\vec{H} e^{-iu}]$, where $\vec{H} = \vec{H}_{(0,0)} + \Sigma \vec{H}_{BF \neq (0,0)}$ denotes the decomposition of the total magnetic field $\vec{H}$, and the phase u is freely adjustable. We select u to minimize the contribution of the incoming propagating mode $BF_{(0,0)}$, ensuring that $|\Re[\vec{H}_{(0,0)} e^{-iu}]| \approx 0$. This approach applies to normal incidence $(\theta = 0, \varphi = 0)$ and, accordingly, to our case, which is nearly normal. Consequently, the resulting plots reveal the C_4 symmetry of the contribution from the excited evanescent modes within these quasi-BICs. The same method was used for the electric field plots. Panels (a, a^*, b, b^*) depict the quasi-BIC at $f_{BIC_{1a}} = 2446.6$ GHz, while panels (A, A^*, B, B^*) correspond to the quasi-BIC at $f_{BIC_{2a}} = 2458.7$ GHz. Here, the index a in $1a$ and $2a$ highlights that these quasi-BICs correspond to the antisymmetric pattern. The phase variable for each panel is given as follows: $(a, u = 90°)$, $(b, u = 0°)$, $(A, u = 130°)$, and $(B, u = 40°)$. Panel (b^*) reveals the vector orientation, which is absent in panel (b) due to the use of the absolute value. In panel (a^*), the magnetic field vector is presented on the plane $x = -60$ μm, which coincides with the vertical y-z plane passing through the center of panel (a). A similar description applies to the panels corresponding to the frequency 2458.7 GHz.

We identified two frequency regions: one hosting a pair of BICs and another where a resonance and a BIC coexist, described by antisymmetric and symmetric transfer matrix patterns, respectively. The infinite Q-factor property is linked to Fano resonances, described as a linear fractional function of frequency. As quasi-BICs approach BICs, the distance between the zero and the pole in this function shrinks, resulting in an infinite Q factor.

Our method extends beyond the specific device studied here, offering clear interpretations through equations that link geometrical parameters and frequencies. It is computationally efficient and can guide the search for BICs in complex photonic structures, especially for very narrow bandwidth quasi-BICs, where full-wave numerical simulations encounter limitations. The precise analytical solutions we present can serve as benchmarks for more complex numerical models.

Future work will explore BICs away from the Gamma-point and in devices with nonsquare unit cells. Further investigation into the topological properties, dispersion relations, and BIC classification are additional avenues for research.

ACKNOWLEDGMENT

APPENDIX: SYMBOLIC FORMULAS FOR THE POLES OF THE ANTISYMMETRIC PATTERN

$$p_1 = r_{W2} - 2\theta^2 \frac{2(B_{14}B_{21} - A_{11}\mu_{24})\mu_{42} + B_{12}[2B_{41}\mu_{24} + B_{21}(\mu_{22} + \mu_{32} - \mu_{44} - \mu_{54})]}{(\beta_{22} + \beta_{32})[2B_{12}B_{21} + 2B_{14}B_{41} + A_{11}(\mu_{22} + \mu_{32} - \mu_{44} - \mu_{54})]}, \tag{A1}$$

$$p_2 = r_{W4} + 2\theta^2 \frac{2(B_{12}B_{41} - A_{11}\mu_{42})\mu_{24} + B_{14}[2B_{21}\mu_{42} + B_{41}(-\mu_{22} - \mu_{32} + \mu_{44} + \mu_{54})]}{(\beta_{22} + \beta_{32})[2B_{12}B_{21} + 2B_{14}B_{41} + A_{11}(-\mu_{22} - \mu_{32} + \mu_{44} + \mu_{54})]}, \tag{A2}$$

where r_{W2} and r_{W4} are the roots of Δ_a corresponding to the diagonal matrix elements (2,2) and (3,3) in Eq. (23):

$$r_{W2} = -\theta^2 \frac{\mu_{22} + \mu_{32}}{\beta_{22} + \beta_{32}}, \tag{A3}$$

$$r_{W4} = -\theta^2 \frac{\mu_{44} + \mu_{54}}{\beta_{22} + \beta_{32}}. \tag{A4}$$

[1] B. Zhen, C. W. Hsu, L. Lu, A. D. Stone, and M. Soljačić, Topological nature of optical bound states in the continuum, Phys. Rev. Lett. **113**, 257401 (2014).

[2] L. Huang, L. Xu, D. A. Powell, W. J. Padilla, and A. E. Miroshnichenko, Resonant leaky modes in all-dielectric meta-systems: Fundamentals and applications, Phys. Rep. **1008**, 1 (2023).

[3] C. Blanchard, J.-P. Hugonin, and C. Sauvan, Fano resonances in photonic crystal slabs near optical bound states in the continuum, Phys. Rev. B **94**, 155303 (2016).

[4] A. Kodigala, T. Lepetit, Q. Gu, B. Bahari, Y. Fainman, and B. Kanté, Lasing action from photonic bound states in continuum, Nature (London) **541**, 196 (2017).

[5] A. Zalogina, L. Carletti, A. Rudenko, J. V. Moloney, A. Tripathi, H.-C. Lee, I. Shadrivov, H.-G. Park, Y. Kivshar, and S. S. Kruk, High-harmonic generation from a subwavelength dielectric resonator, Sci. Adv. **9**, eadg2655 (2023).

[6] F. Yesilkoy, E. R. Arvelo, Y. Jahani, M. Liu, A. Tittl, V. Cevher, Y. Kivshar, and H. Altug, Ultrasensitive hyperspectral imaging and biodetection enabled by dielectric metasurfaces, Nat. Photonics **13**, 390 (2019).

[7] M. Kang, T. Liu, C. Chan, and M. Xiao, Applications of bound states in the continuum in photonics, Nat. Rev. Phys. **5**, 659 (2023).

[8] J. M. Foley, S. M. Young, and J. D. Phillips, Symmetry-protected mode coupling near normal incidence for narrow-band transmission filtering in a dielectric grating, Phys. Rev. B **89**, 165111 (2014).

[9] D. A. Bykov, E. A. Bezus, and L. L. Doskolovich, Coupled-wave formalism for bound states in the continuum in guided-mode resonant gratings, Phys. Rev. A **99**, 063805 (2019).

[10] S. Li, C. Zhou, T. Liu, and S. Xiao, Symmetry-protected bound states in the continuum supported by all-dielectric metasurfaces, Phys. Rev. A **100**, 063803 (2019).

[11] M. S. Sidorenko, O. N. Sergaeva, Z. F. Sadrieva, C. Roques-Carmes, P. S. Muraev, D. N. Maksimov, and A. A. Bogdanov, Observation of an accidental bound state in the continuum in a chain of dielectric disks, Phys. Rev. Appl. **15**, 034041 (2021).

[12] A. Abdrabou, L. Yuan, W. Lu, and Y. Y. Lu, Parametric dependence of bound states in the continuum: A general theory, Phys. Rev. A **107**, 033511 (2023).

[13] D. A. Bykov, E. A. Bezus, A. A. Mingazov, and L. L. Doskolovich, Algebraic approach to finding the number of parameters required to obtain a bound state in the continuum, Phys. Rev. A **109**, 053525 (2024).

[14] C. W. Hsu, B. Zhen, A. D. Stone, J. D. Joannopoulos, and M. Soljačić, Bound states in the continuum, Nat. Rev. Mater. **1**, 16048 (2016).

[15] K. L. Koshelev, Z. F. Sadrieva, A. A. Shcherbakov, Y. S. Kivshar, and A. A. Bogdanov, Bound states in the continuum in photonic structures, Phys. Usp. **66**, 494 (2023).

[16] J. Jin, X. Yin, L. Ni, M. Soljačić, B. Zhen, and C. Peng, Topologically enabled ultrahigh-q guided resonances robust to out-of-plane scattering, Nature (London) **574**, 501 (2019).

[17] O.-Z. Lipan and A. De Sabata, Optimizing bi-layered periodic structures: A closed-form transfer matrix method based on Pendry-MacKinnon's discrete Maxwell's equations, J. Opt. Soc. Am. B **41**, A116 (2024).

[18] O.-Z. Lipan and A. De Sabata, Closed-form analytical solution for the transfer matrix based on Pendry-MacKinnon discrete Maxwell's equations, Opt. Express **33**, 3777 (2025).

[19] W. R. Inc., Mathematica, Version 14, Champaign, IL, 2023.

[20] CST Microwave Studio (Version 2024), Dassault Systmes, 2024, https://www.3ds.com/products-services/simulia/products/cst-studio-suite/.

[21] W. Wang, Y. K. Srivastava, T. C. Tan, Z. Wang, and R. Singh, Brillouin zone folding driven bound states in the continuum, Nat. Commun. **14**, 2811 (2023).

[22] H. Zhong, L. Huang, S. Li, C. Zhou, S. You, L. Li, Y. Cheng, and A. E. Miroshnichenko, Toroidal dipole bound states in the continuum in asymmetric dimer metasurfaces, Appl. Phys. Rev. **11**, 031404 (2024).

[23] D. R. Abujetas, N. Van Hoof, S. ter Huurne, J. Gómez Rivas, and J. A. Sánchez-Gil, Spectral and temporal evidence of robust photonic bound states in the continuum on terahertz metasurfaces, Optica **6**, 996 (2019).

[24] J. B. Pendry and A. MacKinnon, Calculation of photon dispersion relations, Phys. Rev. Lett. **69**, 2772 (1992).

[25] N. Shubin, Algebraic approach to annihilation and repulsion of bound states in the continuum in finite systems, J. Math. Phys. **64**, 042103 (2023).

[26] C. E. J. Png and Y. Akimov, *Nanophotonics and Plasmonics: An Integrated View* (CRC Press, Boca Raton, FL, 2017).

[27] G. W. Roberts and A. S. Sedra, A general class of current amplifier-based biquadratic filter circuits, in *Proceedings of the IEEE International Symposium on Circuits and Systems* (IEEE, Piscataway, NJ, 1991), pp. 1821–1824.

[28] R. Gibson, I. Avrutsky, S. Vangala, D. E. Walker, and J. R. Hendrickson, Pole-based analysis of coupled modes in metal–insulator–metal plasmonic structures, J. Opt. Soc. Am. B **38**, 776 (2021).

[29] M. Nevière, E. Popov, and R. Reinisch, Electromagnetic resonances in linear and nonlinear optics: Phenomenological study of grating behavior through the poles and zeros of the scattering operator, J. Opt. Soc. Am. A **12**, 513 (1995).

[30] I. Avrutsky, R. Gibson, J. Sears, G. Khitrova, H. M. Gibbs, and J. Hendrickson, Linear systems approach to describing and classifying Fano resonances, Phys. Rev. B **87**, 125118 (2013).

[31] V. Grigoriev, A. Tahri, S. Varault, B. Rolly, B. Stout, J. Wenger, and N. Bonod, Optimization of resonant effects in nanostructures via Weierstrass factorization, Phys. Rev. A **88**, 011803(R) (2013).

[32] R. G. Newton, *Scattering Theory of Waves and Particles* (Springer Science & Business Media, Cham, 2013).

[33] E. Mikheeva, R. Colom, K. Achouri, A. Overvig, F. Binkowski, J.-Y. Duboz, S. Cueff, S. Fan, S. Burger, A. Alù *et al.*, Asymmetric phase modulation of light with parity-symmetry broken metasurfaces, Optica **10**, 1287 (2023).

[34] V. Grigoriev, S. Varault, G. Boudarham, B. Stout, J. Wenger, and N. Bonod, Singular analysis of Fano resonances in plasmonic nanostructures, Phys. Rev. A **88**, 063805 (2013).